Holes in silicon are heavier than expected: transport properties of extremely high mobility electrons and holes in silicon MOSFETs

J. P. Wendoloski,[1] J. Hillier,[1] S. D. Liles,[1] M. Rendell,[1] Y. Ashlea-Alava,[1] B. Raes,[2] R. Li,[2,*] S. Kubicek,[2] C. Godfrin,[2] J. Jussot,[2] S. Beyne,[2] D. Wan,[2] Md. M. Rahman,[3] S. Yianni,[3,4,5] K. W. Chan,[3,4] F. E. Hudson,[3,4] W. H. Lim,[3,4] K. De Greve,[2,6] A. S. Dzurak,[3,4] and A. R. Hamilton[1,†]

[1] *School of Physics, University of New South Wales, New South Wales 2052, Australia*
[2] *IMEC, Remisebosweg 1, B-3001 Leuven, Belgium*
[3] *School of Electrical Engineering and Telecommunications, University of New South Wales, New South Wales 2052, Australia*
[4] *Diraq, Sydney, NSW, Australia*
[5] *Université Grenoble Alpes, CEA, Grenoble INP, IRIG, PHELIQS, 38000 Grenoble, France*
[6] *Department of Electrical Engineering (ESAT), KU Leuven, Leuven, Belgium*

(Dated: March 3, 2025)

arXiv:2502.21173v1 [cond-mat.mes-hall] 28 Feb 2025

The quality of the silicon-oxide interface plays a crucial role in fabricating reproducible silicon spin qubits. In this work we characterize interface quality by performing mobility measurements on silicon Hall bars. We find a peak electron mobility of nearly $40,000\,\mathrm{cm^2/Vs}$ in a device with a 21 nm oxide layer, and a peak hole mobility of about $2,000\,\mathrm{cm^2/Vs}$ in a device with 8 nm oxide, the latter being the highest recorded mobility for a p-type silicon MOSFET. Despite the high device quality, we note an order-of-magnitude difference in mobility between electrons and holes. By studying additional n-type and p-type devices with identical oxides, and fitting to transport theory, we show that this mobility discrepancy is due to valence band nonparabolicity. The nonparabolicity endows holes with a density-dependent transverse effective mass ranging from $0.6m_0$ to $0.7m_0$, significantly larger than the usually quoted bend-edge mass of $0.22m_0$. Finally, we perform magnetotransport measurements to extract momentum and quantum scattering lifetimes.

I. INTRODUCTION

Silicon quantum dots offer a promising path towards scalable quantum computing. This is due to their compatibility with existing semiconductor fabrication techniques, as such spin qubits are created using gate-defined potential wells in metal-oxide-semiconductor (MOS) interfaces. The spins of both electrons and holes have been used within this approach. Electron spins have received significant attention due to their long coherence times in silicon [1–6]. Likewise, holes show promise due to their intrinsic spin-orbit coupling, enabling fast all-electrical control of the spin state [7–16]. In both cases, this approach requires the fabrication of millions of these qubits, which relies on the ability to create very low disorder MOS interfaces.

Transport measurements performed on Hall bars have been used to characterise the disorder of n-type MOS interfaces at low temperatures [17–19]. The charge carrier mobility is a key metric used to assess interface quality, and theoretical models can be used to infer interface characteristics from the measured mobility [17, 20]. Correspondingly, studies of hole mobility can yield valuable information about p-type interface quality, which is instrumental in the pursuit of large numbers of hole spin qubits. Whereas low temperature mobilities in excess of $30,000\,\mathrm{cm^2/Vs}$ have been reported for electrons at MOS interfaces [18, 21], reported hole mobilities tend to be an order of magnitude lower [22, 23]. This is somewhat unexpected, given that the often-cited hole transverse effective mass $0.22m_0$ is only slightly larger than the electron transverse effective mass $0.19m_0$ (appendix B). It is important to identify the cause of this low hole mobility, and whether it reflects a difference in disorder that could be detrimetal to formation of hole qubit devices, or is some other effect.

To study this mobility discrepancy we measure two pairs of comparable n-type and p-type Hall bars. One pair of devices is fabricated on a 300-mm wafer at IMEC, and the other is fabricated using academic cleanroom facilities at UNSW. The IMEC samples show the highest electron and hole mobilities in a thin oxide silicon MOSFET, while the UNSW samples provide a direct comparison between electron and hole mobilities on wafers with nominally identical oxides. Across both pairs of devices, we observe hole mobilities that are roughly an order of magnitude lower than the corresponding electron mobilities. Although the band edge mobilities for electrons and holes are similar, here we show that the mobility difference can be explained by the highly non-parabolic nature of the valence band. This nonparabolicity results in a large enhancement of the hole transverse effective mass at Fermi energies relevant to typical transport and spin qubit measurements [24]. Using this more accurate treatment of the hole mass, we succeed in explaining the observed differences in mobility and confirm that the oxide quality for MOS

* now at Applied Materials, Inc.
† Alex.Hamilton@unsw.edu.au

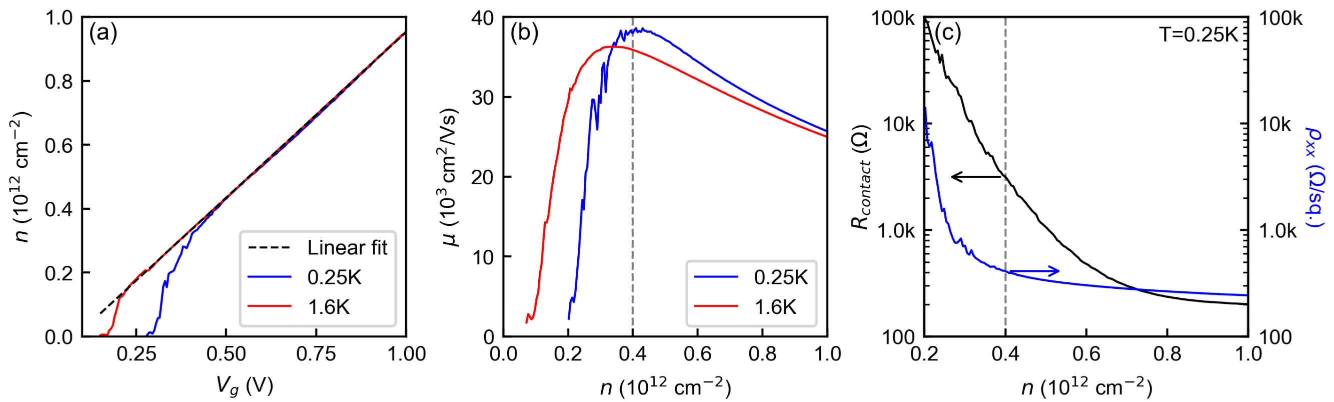

FIG. 1. (a) Carrier density n as a function of gate voltage V_g at temperatures 0.25 K and 1.6 K. A linear fit to the 1.6 K data yielding an oxide thickness of $t_{\rm ox} = 20.8\,$nm is included. (Both curves produce virtually identical fits.) (b) Carrier mobility μ as a function of density at 0.25 K and 1.6 K. A peak mobility $\mu = 38,600\,{\rm cm}^2/{\rm Vs}$ at 0.25 K is achieved at a density $n \simeq 0.4 \times 10^{12}\,{\rm cm}^{-2}$. (c) Contact resistance $R_{\rm contact}$ and resistivity ρ_{xx} measured as a function of density at 0.25 K. At the peak mobility, $R_{\rm contact} = 3.2\,{\rm k}\Omega$ and $\rho_{xx} = 410\,\Omega/{\rm sq.}$.

devices is comparable for electrons and holes.

II. IMEC ELECTRON MOBILITY MEASUREMENTS

We begin by measuring a high-quality n-type silicon MOSFET with a 21 nm oxide layer, fabricated by IMEC [17, 18]. In all our measurements, we used standard lock-in techniques and a 4-point probe setup, applying a source-drain voltage of $100\,\mu$V at 33 Hz. Fig. 1 illustrates results for the n-type IMEC device. We calculate the carrier density n by measuring the Hall voltage V_{xy} at five magnetic fields from -0.5 T to $+0.5$ T.

The extracted density is shown as a function of gate voltage V_g in Fig. 1 (a). We find a linear relationship between density and gate voltage, as expected for a MOSFET. Assuming a relative permittivity $\kappa_{\rm ox} = 3.9$ for the silicon oxide, we calculate an oxide thickness of $t_{\rm ox} = 20.8\,$nm, in agreement with the oxide thickness of 21 nm specified in the fabrication process.

At low carrier densities and low temperatures, there is a deviation in the linear relationship between the gate voltage and the carrier density extracted from the Hall effect. This may be due to the narrow width of the Hall probes, and/or the onset of percolation [25]. Similar deviations were observed for all the n-type and p-type devices. Because we still expect the MOS interface to function as a capacitor in this regime, we assume a linear relationship between n and V_g for all further analysis.

From the resistivity ρ_{xx} and carrier density, we calculate the carrier mobility μ, shown as a function of density in Fig. 1 (b). At a temperature of 0.25 K we find a peak mobility of nearly $40,000\,{\rm cm}^2/{\rm Vs}$, the highest of any thin oxide ($<100\,$nm) Si/SiO$_2$ MOSFET. Finally, Fig. 1 (c) shows the contact resistance and resistivity. The contact resistance is calculated from the difference between the total resistance across the device and the longitudinal resistivity ρ_{xx}, appropriately considering the device geometry. At $n = 0.4 \times 10^{12}\,{\rm cm}^{-2}$ and 0.25 K, we find a contact resistance of only $3\,{\rm k}\Omega$.

III. IMEC ELECTRON AND HOLE MOBILITIES

To compare electron and hole mobilities, we measured a p-type silicon MOSFET from IMEC with a 8 nm oxide, fabricated in the same process as the 21 nm n-type MOSFET [17, 18]. We expect the interface roughness characteristics to be similar between n-type and p-type devices, as they are fabricated in nominally identical processes with the disorder determined by the average microscopic structure of the interface. The Coulomb impurity scattering could be different between n-type and p-type devices, due to the different oxide thicknesses (8 nm and 20 nm), which moves the top surface further from the 2D channel in the n-type devices [18]. Because scattering in the high density limit is dominated by interface roughness (section IV), we expect the disorder to be comparable within this regime.

Figure 2 shows the mobility of both devices as a function of density, measured at 1.6 K. We find peak electron and hole mobilities of $36,000\,{\rm cm}^2/{\rm Vs}$ and $2,100\,{\rm cm}^2/{\rm Vs}$ respectively, the latter being the highest recorded mobility for a p-type silicon MOSFET. Despite this, the hole mobility is still an order-of-magnitude lower than the electron mobility at the same temperature. This is unexpected, given that the transverse component of the

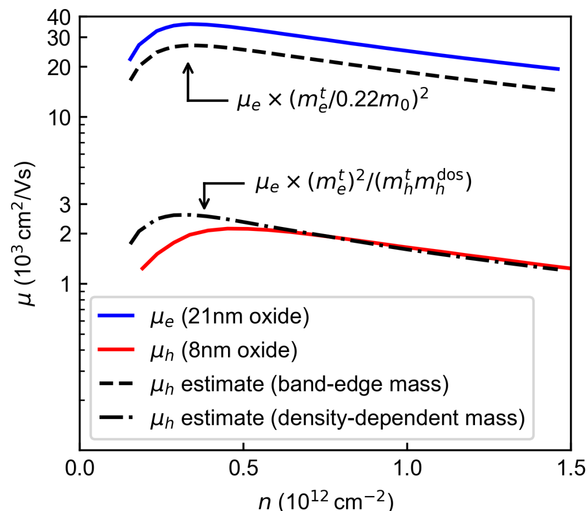

FIG. 2. Measured electron mobility μ_e and hole mobility μ_h of the IMEC devices at 1.6 K, with peak mobilities of $36,000\,\mathrm{cm}^2/\mathrm{Vs}$ and $2,100\,\mathrm{cm}^2/\mathrm{Vs}$ respectively. The dashed and dash-dotted lines show the predicted mobility for holes using the band-edge effective mass $0.22m_0$ and the density-dependent effective masses from Ref. [24] respectively.

hole effective mass $0.22m_0$ is only slightly larger than the electron effective mass $m_e^t = 0.19m_0$.

This discrepancy occurs because the hole effective mass $0.22m_0$ is inapplicable at the Fermi energies occurring in this experiment; nonparabolicity of the valence band means that the value $0.22m_0$ is only valid in an extremely limited region around $n = 0$. While such nonparabolicity would generally require a more sophisticated calculation [26], Ref. [24] shows how multiple density-dependent effective masses may be used to model transport in these conditions. At densities of $n \sim 10^{12}\,\mathrm{cm}^{-2}$, which are relevant to our measurements and hole-spin qubit operation [9], a transverse effective mass m_h^t ranging from $0.6m_0$ to $0.7m_0$ and a density-of-states effective mass m_h^{dos} ranging from $0.7m_0$ to $0.9m_0$ may be introduced (see appendix B and C).

We investigate if this effective mass can explain the difference between the measured electron and hole mobilities. Mobility is approximately related to effective mass via $\mu \propto 1/m^2$, where mass dependence arises due to (a) the relationship between mobility and momentum relaxation time, and (b) the relationship between momentum relaxation time and scattering matrix elements. Note that this approximation is suited to the high-density limit where temperature dependent screening (which introduces additional m dependence) becomes unimportant.

The dashed curve in Fig. 2 shows the hole mobility that is expected by scaling the electron mobility with the square of the band-edge effective masses, that is

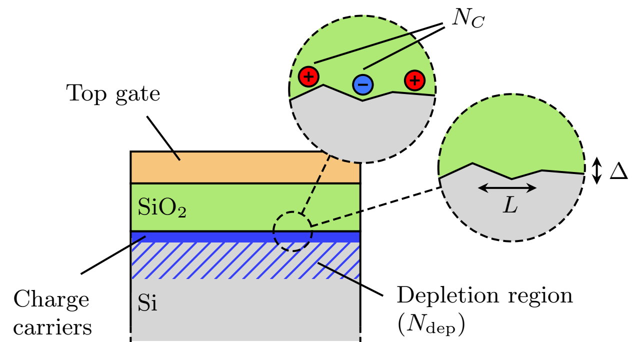

FIG. 3. Schematic diagram of a silicon MOSFET. A sheet of charge carriers flows beneath the Si/SiO_2 interface. Charged impurities (characterised by N_C) and interface roughness (characterised by Δ and L) cause the charge carriers to scatter. A depletion layer wth density N_{dep} forms beneath the system.

$\mu_e \times (m_e^t/0.22m_0)^2$. Similarly, the dash dotted curve in Fig. 2 also shows the expected hole mobility, but using the heavier hole masses arising from the band nonparabolicity. The latter curve is a much closer fit to the measured hole mobilities, suggesting that the low hole mobility is a result of the large density-dependent hole mass.

IV. THEORETICAL MOBILITY ANALYSIS

To understand the microscopic factors limiting the mobility we use the theoretical analysis of Kruithof, Klapwijk and Bakker (KKB) [17, 20]. The KKB model considers scattering from charged impurities and roughness at the MOS interface, as illustrated in Fig. 3.

Five different parameters are used to characterise the MOSFET. First is the density of charged impurities, denoted by N_C. For simplicity these charges are assumed to lie exactly at the interface, and dominate the scattering at low carrier densities. Next, the interface roughness is described by Δ and L, which represent the amplitude and correlation length respectively. At higher carrier densities the confining electric field pulls the carriers up against the Si/SiO_2 interface, increasing the strength of the interface roughness scattering.

Depletion charge in the silicon substrate is also considered. This charge increases the electric field at the interface, amplifying the effect of interface roughness scattering. The increase in electric field also changes the shape of the confining potential and the Fang-Howard wavefunction, affecting both screening and charged impurity scattering. The two-dimensional depletion charge density is given by N_{dep}, with the sign of the depletion charge taken to match the mobile charge carriers.

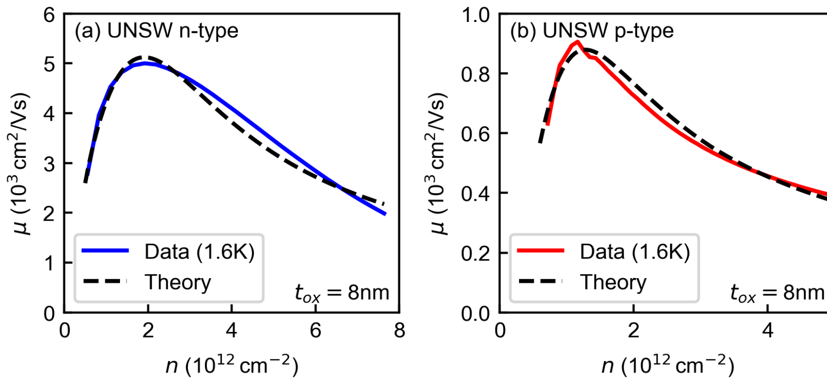

FIG. 4. (a) Measured and theoretical carrier mobilities for the UNSW fabricated n-type device. The $T = 0$ theoretical model has been fit to both the n-type and p-type mobility curves simultaneously, with the density-dependent hole masses used for the p-type device. (b) Measured and theoretical carrier mobilities for the p-type device.

Parameter	n-type	p-type
N_C ($10^{10}\,\mathrm{cm}^{-2}$)	5.1 ± 0.3	—"—
Δ (nm)	0.39 ± 0.01	—"—
L (nm)	3.7 ± 0.4	—"—
σ (meV)	1.7 ± 0.4	—"—
N_{dep} ($10^{12}\,\mathrm{cm}^{-2}$)	0.00 ± 0.01	0.15 ± 0.02

TABLE I. Parameter values for the fits in figure 4. The values of N_C, Δ, L and σ are identical for both mobility curves.

Finally, the band-tailing parameter σ models the reduction in available states at low carrier densities n. Here we leave it as a free parameter, but it might be expected to be related to the disorder at low density, arising from the charged impurity density N_C [20, 27].

When generalising the model to hole mobilities, the effective mass and absence of valley degeneracy must be considered. The density-dependent effective mass defined in Ref. [24] is straightforward to incorporate. The larger effective mass acts to slow down the carriers, and increase the number of states they scatter into. The absence of valley degeneracy also reduces mobility, by reducing the effects of screening via the density of states. However, the overall effect on screening is not large, as the increased effective mass and absence of valley degeneracy cancel out somewhat. We provide full details of the generalised model in appendix C.

V. UNSW ELECTRON AND HOLE MOBILITIES

To unambiguously prove that the difference in mobility between electrons and holes is due to the density dependent hole mass, we fabricated and tested a second set of n-type and p-type Hall bars. These devices were fabricated at UNSW in a laboratory setting. Importantly, both devices were fabricated with a nominally identical 8 nm oxide thickness. As such, we expect that their interfaces are described by a similar set of parameters in the KKB model (generalised using the density-dependent hole mass).

Mobility curves for the n-type and p-type UNSW devices are shown in Fig. 4 (a) and (b) respectively. Similar to before, there is roughly an order-of-magnitude difference between the measured n-type and p-type mobilities. We fit the generalised KKB model to both the n-type and p-type curves simultaneously, under the constraint that N_C, Δ, L and σ are the same for both mobility curves. The fitted curves are shown in Fig. 4, and the parameters are summarised in table I. We succeed in fitting to the both electron and hole mobility curves using these common parameters, demonstrating that the density-dependent hole mass explains the order-of-magnitude difference in mobility. Note that the UNSW devices have negligible temperature dependence, with less than a 2% variation in peak mobility between 1.6 K and 5.6 K measurements. Therefore, we ignore temperature in our theoretical modelling.

The only parameter we allowed to vary between devices was the depletion charge density, which is zero for the n-type device and slightly non-zero for the p-type device. This is consistent with slight n-type doping in the silicon substrate. While some depletion charge seems necessary to explain the difference in mobility, zeroing this parameter increases the p-type device mobility by only 20%.

VI. MAGNETORESISTANCE MEASUREMENTS

Finally, to build upon the mobility measurements, for completeness we also examine the Shubnikov-de Haas oscillations in the magnetoresistance of the n-type IMEC and UNSW devices for multiple carrier densities, at a temperature of 1.6 K. (We did not observe significant oscillations in our p-type devices at $T = 1.6$ K and magnetic fields up to $B = 5$ T.) These measurements allow us to independently confirm the carrier density, determine the quantum (Dingle) scattering time for the

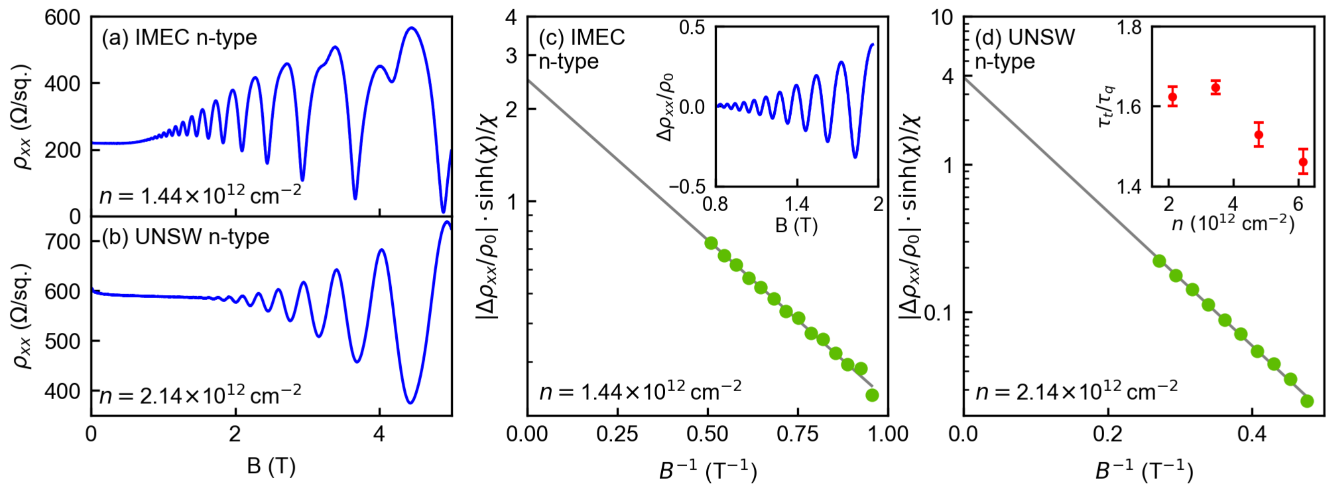

FIG. 5. (a) Longitudinal resistivity ρ_{xx} as a function of magnetic field B at 1.6 K and $V_g = 1.5$ V for the IMEC device. The background magnetoresistance shows an unusual upward curvature around 1 T. Same plot at $V_g = 1.0$ V for the UNSW device. Both plots share the same x-axis. (c) Dingle plot of the IMEC device, corresponding to the sweep in (a). The inset shows the scaled resistivity $\Delta\rho_{xx}/\rho_0$ after a background polynomial has been subtracted form the raw ρ_{xx} curve. (d) Dingle plot of the UNSW device, corresponding to the sweep in (b). The inset shows the Dingle ratio τ_t/τ_q, which decreases as the carrier density increases.

2D electrons, and examine how the ratio of the quantum and momentum relaxation times varies with carrier density [28, 29]

Figures 5 (a) and (b) show these oscillations in the IMEC and UNSW samples. The onset of these oscillations occurs earlier in the IMEC sample than in the UNSW one, which is expected due to the higher mobility. Spin splitting is observed in the IMEC sample at roughly 3 T. An unusual feature of the IMEC device is the positive background magnetoresistance around 1 T. By contrast, both the UNSW device and other silicon MOSFETs [17–19] have a flat or negative magnetoresistance.

To extract the quantum scattering lifetime from the oscillations, we compare the measured values of ρ_{xx} to the theoretical values predicted by equation 1 [30]. The resistivity is related to the magnetic field B through the cyclotron frequency ω_c, and the carrier density is related to the Fermi energy via the relations $n = D\cdot\varepsilon_F$ and $D = g_v m_e^t/(\pi\hbar)^2$ where D is the density of states. The quantum lifetime τ_q represents the amount of time between collisions that dephase the electrons. Note that this equation is valid for two-dimensional systems [31].

$$\frac{\Delta\rho_{xx}}{\rho_0} = (-4)\frac{\chi}{\sinh\chi}\cos\left(\frac{2\pi\varepsilon_F}{\hbar\omega_c}\right)\exp\left(-\frac{\pi}{\omega_c\tau_q}\right)$$
$$\chi = \frac{2\pi^2 k_B T}{\hbar\omega_c}, \quad \omega_c = \frac{eB}{m_e^t} \qquad (1)$$

We subtract a background polynomial from the raw ρ_{xx} data to reveal the oscillatory component $\Delta\rho_{xx}$. This process is exemplified in the inset of Fig. 5 (c) for the IMEC device. The frequency of the SdH oscillations provides an independent measure of the carrier density. In all our measurements, this agrees with the density obtains via the low-field Hall effect to within 2%.

Device	V_g (V)	n (10^{12} cm^{-2})	τ_t/τ_q	τ_t/τ_q (constr.)
UNSW	1.0	2.14 ± 0.02	1.62 ± 0.02	—
—"—	1.5	3.49 ± 0.03	1.65 ± 0.02	—
—"—	2.0	4.83 ± 0.05	1.53 ± 0.03	—
—"—	2.5	6.18 ± 0.05	1.46 ± 0.03	—
IMEC	0.7	0.63 ± 0.01	2.7	3.3
—"—	1.1	1.04 ± 0.02	1.9	2.4
—"—	1.5	1.44 ± 0.03	1.5	1.8

TABLE II. Data extracted from the SdH oscillations for the UNSW and IMEC n-type devices. The carrier density n is calculated by averaging the values extracted from the Hall effect and SdH oscillations; the uncertainty reflects the difference between these estimates. For the IMEC device, we calculate Dingle ratios where the intercept is constrained to pass through 4. (The difference between these estimates dominates all other sources of uncertainty.)

We use Dingle plots to calculate the quantum lifetime [30, 32]. These are produced by plotting the magnitude of the peaks and valleys in the temperature-adjusted resistivity $|\Delta\rho_{xx}/\rho_0| \times \sinh\chi/\chi$ against the inverse field $1/B$. This quantity should appear linear on a log plot, and from its gradient we can extract τ_q. Note that equation 1 implies that the intercept of the resultant curve should be 4 [30]. A good Dingle plot should have

this intercept, as shown in Fig. 5 (d).

Good Dingle plots are obtained for the UNSW device at all carrier densities. However, the intercepts for the IMEC devices fall below 4 for each sweep, as shown in Fig. 5 (c). To determine if this significantly affects the extracted quantum lifetimes of the IMEC samples, we consider Dingle plots whose intercepts are constrained to pass through 4. This produces quantum lifetimes which are 20–30% smaller, but still show the same trend with carrier density [33] [34].

From the quantum lifetime, we calculate the Dingle ratio τ_t/τ_q which characterises the typical range of scatterers from the 2DEG. These are summarised in table II for both devices. Larger Dingle ratios indicate that long-range scattering is dominant [28]. For both devices, we find that the Dingle ratio decreases with density. This ratio is plotted for the UNSW device in the inset of Fig. 5 (d). This decreasing ratio is expected in light of scattering theory; at higher densities, short-range interface roughness scattering becomes the dominant scattering mechanism.

VII. CONCLUSION

We measured electron and hole mobilities from two pairs of similarly fabricated silicon MOSFETs, reporting the highest measured mobilities in a thin oxide device. Across both samples we observe hole mobilities that are roughly an order-of-magnitude lower than those of electrons. We show that this is due to valence band non-parabolicity, which leads to a transverse effective mass much larger than $0.22m_0$ at the Fermi energies present in MOSFETs and qubits. Finally, we measured Shubnikov-de Haas oscillations, which we used to extract Dingle ratios and probe the typical range of scatterers in each device.

ACKNOWLEDGMENTS

This work was supported by the Australian Research Council through grant LP200100019 and the US Army Research Office through W911NF-23-10092. K.W.C. and A.R.H. acknowledge ARC Fellowships IM230100396 and IL230100072, co-funded by Diraq Pty Ltd, and A.S.D. acknowledges ARC Fellowship FL190100167. UNSW devices were made at the New South Wales node of the Australian National Fabrication Facility.

COMPETING INTERESTS

A.S.D. is the CEO and a director of Diraq Pty Ltd. K.W.C., F.E.H., W.H.L. and A.S.D. declare equity interest in Diraq Pty Ltd. The remaining authors declare no competing interests.

Appendix A: Device stock numbers

Manufacturer	Oxide (nm)	Carrier	Identifier
IMEC	21	n-type	`AL210563_D06`
IMEC	8	p-type	`AL210563_D07`
Diraq/UNSW	8	n-type	`6ND03`
Diraq/UNSW	8	p-type	`6NI01`

TABLE III. Stock numbers and information about the devices. The sign of the charge carriers is set by the doping of the ohmic contacts.

Appendix B: Effective masses of electrons and holes

The effective mass approximation (EMA) assumes a quadratic relationship between the energy and wavevector of the charge carriers. This approximation simplifies the calculation of transport properties, and provides adequate accuracy in the conduction band of silicon. For the (100) crystal orientation of our devices, two components of the electron effective mass must be considered [35]. First is the transverse component $m_e^t = 0.19m_0$, which largely determines the transport properties of the system. It plays a direct role in determining the density of states, scattering rate and carrier mobility. Second is the vertical component $m_e^z = 0.98m_0$ which determines the energy levels of the quantised subbands that the electrons occupy.

In 2D systems, the silicon valence band is split into heavy hole and light hole components. Transport in silicon MOSFETs at low temperatures is dominated by the heavy hole component [24]. Ref. [36] (p. 48) provide simple calculation instructions for the transverse and vertical components of the heavy hole effective mass. The values obtained are $m_h^t = 0.22m_0$ and $m_h^z = 0.28m_0$.

However, because the valence band is significantly nonparabolic, these hole effective masses are only valid in an extremely limited region around the band-edge. In particular, this nonparabolicity is highly relevant for typical Fermi energies occuring in our devices.

Ref. [24] introduce density-dependent effective masses that model the transport of holes. For heavy holes in (100) oriented silicon, they introduce three such effective masses, shown in Fig. 6. The first of these is the *density of states* effective mass m_h^{dos} which ranges from $0.7m_0$ to $0.9m_0$ at typical carrier densities of $10^{11}\,\mathrm{cm}^{-2}$ to $10^{13}\,\mathrm{cm}^{-2}$. This component is relevant to the density of states and scattering rate calculations. The next is the

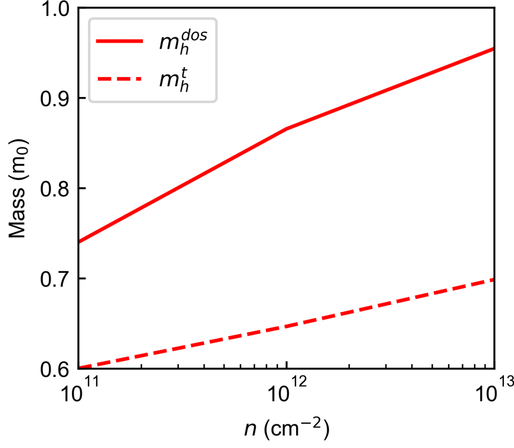

FIG. 6. Effective mass components for holes as a function of carrier density. The vertical component is given by $m_h^z = 0.28m_0$. Reproduced from ref. [24].

transport effective mass m_h^t which ranges from $0.6m_0$ to $0.7m_0$ over the same densities, and plays a direct role in linking the transport lifetime to mobility. The last is the *quantisation* effective mass $m_h^z = 0.27m_0$ which plays the same role as the vertical effective mass in calculating subband energies. It has negligible dependence on the carrier density.

Appendix C: Theoretical mobility model

Here we provide a complete expression of the mobility model used in our calculations. We use the model described in ref. [20] at $T = 0$, generalised to account for hole mobilities.

Table IV defined generalised effective masses for the electrons and holes, where the hole masses are the density-dependent expressions from ref. [24].

Equation C1 introduces the Fermi wave vector k_F, Fermi energy ε_F, and density of states D. These are computed as a function of the carrier density n. The valley degeneracy factor g_v equals 2 for electrons and 1 for holes.

Parameter	Electrons (m_0)	Holes (m_0)
m^t	0.19	(0.6)–(0.7)
m^{dos}	—"—	(0.7)–(0.9)
m^z	0.98	0.28

TABLE IV. Values of effective mass parameters for both electrons and holes. In this notation, m^{dos} and m^t are identical for electrons. The density-dependent hole masses apply for densities between $10^{11}\,\mathrm{cm}^{-2}$ to $10^{13}\,\mathrm{cm}^{-2}$.

$$k_F = \sqrt{\frac{2\pi n}{g_v}}, \quad D = \frac{g_v m^{\mathrm{dos}}}{\pi\hbar^2}, \quad \varepsilon_F = \frac{n}{D} \tag{C1}$$

We also use the relative electric permittivities of the silicon substrate κ_{si}, the silicon oxide κ_{ox}, and their average $\overline{\kappa}$, as shown in equation C2.

$$\kappa_{\mathrm{si}} = 3.9, \quad \kappa_{\mathrm{ox}} = 11.8, \quad \overline{\kappa} = \frac{\kappa_{\mathrm{si}} + \kappa_{\mathrm{ox}}}{2} \tag{C2}$$

Next we introduce the variational parameter b, shown in equation C3. This parameter is related to the thickness of the carrier wavefunction (which equals $3/b$).

$$b = \left[\frac{12e^2 m^z}{\hbar^2\epsilon_0\kappa_{\mathrm{si}}}\left(N_{\mathrm{dep}} + \frac{11}{32}n\right)\right]^{1/3} \tag{C3}$$

Now we may write down the squared matrix element for charged impurity scattering, which is given by equation C4. This equation is the only place where the free parameter N_C enters. The parameter q is the difference in wave vector between the scattered and incoming charge carriers.

$$|W_C(q)|^2 = N_C\left[\frac{e^2}{2\epsilon_0\overline{\kappa}q}\frac{1}{(1+q/b)^3}\right]^2 \tag{C4}$$

Equations C5, C6 and C7 define the interface roughness matrix element. To begin, we introduce the average electric field at the interface E_{avg} in equation C5.

$$E_{\mathrm{avg}} = \frac{e}{\epsilon_0\kappa_{\mathrm{si}}}\left(N_{\mathrm{dep}} + \frac{1}{2}n\right) \tag{C5}$$

Next, equation C6 defines $\widetilde{C}(q)$, the Fourier transform of the correlation function of the interface roughness. This equation is the only place where the free parameters Δ and L enter.

$$\widetilde{C}(q) = \frac{\pi\Delta^2 L^2}{(1+q^2L^2/2)^{3/2}} \tag{C6}$$

Finally, we define the squared matrix element for the interface roughness in equation C7.

$$|W_{IR}(q)|^2 = (eE_{\mathrm{avg}})^2\widetilde{C}(q) \tag{C7}$$

Equations C8, C9 and C10 define the dielectric screening function. We begin by introducing $\widetilde{U}_{\mathrm{int}}(q)$, which is the Fourier transform of the interaction potential of the charge carriers, and is defined by equation C8 [37].

$$\widetilde{U}_{\mathrm{int}}(q) = \frac{e^2}{2\epsilon_0\overline{\kappa}q}F(q), \quad \text{where}$$

$$F(q) = \frac{1}{16}\left(1+\frac{\kappa_{\mathrm{ox}}}{\kappa_{\mathrm{si}}}\right)\frac{(8+9q/b+3q^2/b^2)}{(1+q/b)^3} + \frac{1}{2}\left(1-\frac{\kappa_{\mathrm{ox}}}{\kappa_{\mathrm{si}}}\right)\frac{1}{(1+q/b)^6}. \tag{C8}$$

The form factor $F(q)$ in equation C8 accounts for the nonzero thickness of the carrier wavefunction. (Note that $F(q) \to 1$ as $1/b \to 0$.)

Next, equation C9 defined the factor $G(q)$, which is a correction to the screening at low carrier densities.

$$G(q) = \frac{1}{2g_v} \frac{q}{\sqrt{q^2 + k_F^2}} \tag{C9}$$

The dielectric screening function is then defined in C10. The term $\mathrm{erf}(\varepsilon_F/\sigma\sqrt{2})$ accounts for the reduction in density-of-states at low carrier densities. (The error function is an approximation to a more detailed self-consistent calculation given in ref. [20].)

$$\epsilon(q) = 1 + D \cdot \widetilde{U}_{\mathrm{int}}(q)(1 - G(q))\mathrm{erf}\left(\frac{\varepsilon_F}{\sigma\sqrt{2}}\right) \tag{C10}$$

The scattering matrix elements and dielectric screening function are combined to obtain the $T = 0$ scattering rate, shown in equation C11. We integrate over the scattering angle θ in this expression, which we found suitable for our numerical methods.

$$\begin{gathered} \frac{1}{\tau_t} = \frac{m^{\mathrm{dos}}}{\pi\hbar^3} \int_0^\pi d\theta \, (1 - \cos\theta) \frac{|W_C(q)|^2 + |W_{IR}(q)|^2}{\epsilon(q)^2} \\ q = k_F \sqrt{2(1 - \cos\theta)} \end{gathered} \tag{C11}$$

Finally, the carrier mobility μ is related to the transport lifetime via equation C12.

$$\mu = \frac{e\tau_t}{m^t}. \tag{C12}$$

[1] M. Veldhorst, C. H. Yang, J. C. C. Hwang, W. Huang, J. P. Dehollain, J. T. Muhonen, S. Simmons, A. Laucht, F. E. Hudson, K. M. Itoh, *et al.*, A two-qubit logic gate in silicon, Nature **526**, 410 (2015).

[2] M. F. Gonzalez-Zalba, S. De Franceschi, E. Charbon, T. Meunier, M. Vinet, and A. S. Dzurak, Scaling silicon-based quantum computing using CMOS technology, Nature Electronics **4**, 872 (2021).

[3] J. Y. Huang, R. Y. Su, W. H. Lim, M. Feng, B. van Straaten, B. Severin, W. Gilbert, N. Dumoulin Stuyck, T. Tanttu, S. Serrano, *et al.*, High-fidelity spin qubit operation and algorithmic initialization above 1 K, Nature **627**, 772 (2024).

[4] R. Maurand, X. Jehl, D. Kotekar-Patil, A. Corna, H. Bohuslavskyi, R. Laviéville, L. Hutin, S. Barraud, M. Vinet, M. Sanquer, and S. De Franceschi, A CMOS silicon spin qubit, Nature communications **7**, 13575 (2016).

[5] M. Veldhorst, J. C. C. Hwang, C. H. Yang, A. W. Leenstra, B. de Ronde, J. P. Dehollain, J. T. Muhonen, F. E. Hudson, K. M. Itoh, A. Morello, and A. S. Dzurak, An addressable quantum dot qubit with fault-tolerant control-fidelity, Nature nanotechnology **9**, 981 (2014).

[6] P. C. Spruijtenburg, S. V. Amitonov, W. G. Van Der Wiel, and F. A. Zwanenburg, A fabrication guide for planar silicon quantum dot heterostructures, Nanotechnology **29**, 143001 (2018).

[7] D. V. Bulaev and D. Loss, Electric dipole spin resonance for heavy holes in quantum dots, Physical review letters **98**, 097202 (2007).

[8] A. Crippa, R. Maurand, L. Bourdet, D. Kotekar-Patil, A. Amisse, X. Jehl, M. Sanquer, R. Laviéville, H. Bohuslavskyi, *et al.*, Electrical spin driving by g-matrix modulation in spin-orbit qubits, Physical review letters **120**, 137702 (2018).

[9] S. D. Liles, R. Li, C. H. Yang, F. E. Hudson, M. Veldhorst, A. S. Dzurak, and A. R. Hamilton, Spin and orbital structure of the first six holes in a silicon metal-oxide-semiconductor quantum dot, Nature communications **9**, 3255 (2018).

[10] F. N. M. Froning, L. C. Camenzind, O. A. H. van der Molen, A. Li, E. P. A. M. Bakkers, D. M. Zumbühl, and F. R. Braakman, Ultrafast hole spin qubit with gate-tunable spin–orbit switch functionality, Nature Nanotechnology **16**, 308 (2021).

[11] S. D. Liles, F. Martins, D. S. Miserev, A. A. Kiselev, I. D. Thorvaldson, M. J. Rendell, I. K. Jin, F. E. Hudson, M. Veldhorst, K. M. Itoh, *et al.*, Electrical control of the g tensor of the first hole in a silicon MOS quantum dot, Physical Review B **104**, 235303 (2021).

[12] L. C. Camenzind, S. Geyer, A. Fuhrer, R. J. Warburton, D. M. Zumbühl, and A. V. Kuhlmann, A hole spin qubit in a fin field-effect transistor above 4 kelvin, Nature Electronics **5**, 178 (2022).

[13] I. K. Jin, K. Kumar, M. J. Rendell, J. Y. Huang, C. C. Escott, F. E. Hudson, W. H. Lim, A. S. Dzurak, A. R. Hamilton, and S. D. Liles, Combining n-MOS charge sensing with p-MOS silicon hole double quantum dots in a CMOS platform, Nano Letters **23**, 1261 (2023).

[14] C. X. Yu, S. Zihlmann, J. C. Abadillo-Uriel, V. P. Michal, N. Rambal, H. Niebojewski, T. Bedecarrats, M. Vinet, É. Dumur, M. Filippone, *et al.*, Strong coupling between a photon and a hole spin in silicon, Nature Nanotechnology **18**, 741 (2023).

[15] S. D. Liles, D. J. Halverson, Z. Wang, A. Shamim, R. S. Eggli, I. K. Jin, J. Hillier, K. Kumar, I. Vorreiter, M. Rendell, *et al.*, A singlet-triplet hole-spin qubit in MOS silicon, arXiv preprint arXiv:2310.09722 (2023).

[16] Z. Wang, A. Sarkar, S. D. Liles, A. Saraiva, A. S. Dzurak, A. R. Hamilton, and D. Culcer, Electrical operation of hole spin qubits in planar MOS silicon quantum dots, Physical Review B **109**, 075427 (2024).

[17] T. N. Camenzind, A. Elsayed, F. A. Mohiyaddin, R. Li, S. Kubicek, J. Jussot, P. Van Dorpe, B. Govoreanu, I. Radu, and D. M. Zumbühl, High mobility Si MOSFETs fabricated in a full 300 mm CMOS process, Materials for Quantum Technology **1**, 041001 (2021).

[18] A. Elsayed, M. Shehata, C. Godfrin, S. Kubicek, S. Massar, Y. Canvel, J. Jussot, G. Simion, M. Mongillo, D. Wan, *et al.*, Low charge noise quantum dots with industrial CMOS manufacturing, npj Quantum Information (2024).

[19] D. Sabbagh, N. Thomas, J. Torres, R. Pillarisetty, P. Amin, H. C. George, K. Singh, A. Budrevich, M. Robinson, D. Merrill, *et al.*, Quantum transport properties of industrial $^{28}Si/^{28}SiO_2$, Physical Review Applied **12**, 014013 (2019).

[20] G. H. Kruithof, T. M. Klapwijk, and S. Bakker, Temperature and interface-roughness dependence of the electron mobility in high-mobility Si (100) inversion layers below 4.2K, Physical Review B **43**, 6642 (1991).

[21] S. V. Kravchenko, G. V. Kravchenko, J. E. Furneaux, V. M. Pudalov, and M. d'Iorio, Possible metal-insulator transition at $B = 0$ in two dimensions, Physical Review B **50**, 8039 (1994).

[22] A. C. Betz, M. F. Gonzalez-Zalba, G. Podd, and A. J. Ferguson, Ambipolar quantum dots in intrinsic silicon, Applied Physics Letters **105** (2014).

[23] F. Mueller, G. Konstantaras, W. G. van der Wiel, and F. A. Zwanenburg, Single-charge transport in ambipolar silicon nanoscale field-effect transistors, Applied physics letters **106** (2015).

[24] L. Donetti, F. Gamiz, S. Thomas, T. E. Whall, D. R. Leadley, P.-E. Hellstrom, G. Malm, and M. Ostling, Hole effective mass in silicon inversion layers with different substrate orientations and channel directions, Journal of Applied Physics **110** (2011).

[25] L. A. Tracy, E. H. Hwang, K. Eng, G. A. Ten Eyck, E. P. Nordberg, K. Childs, M. S. Carroll, M. P. Lilly, and S. D. Sarma, Observation of percolation-induced two-dimensional metal-insulator transition in a Si MOSFET, Physical Review B **79**, 235307 (2009).

[26] E. Marcellina, A. Hamilton, R. Winkler, and D. Culcer, Spin-orbit interactions in inversion-asymmetric two-dimensional hole systems: A variational analysis, Physical Review B **95**, 075305 (2017).

[27] E. Arnold, Conduction mechanisms in bandtails at the Si/SiO_2 interface, Surface Science **58**, 60 (1976).

[28] S. J. MacLeod, K. Chan, T. P. Martin, A. R. Hamilton, A. See, A. P. Micolich, M. Aagesen, and P. E. Lindelof, Role of background impurities in the single-particle relaxation lifetime of a two-dimensional electron gas, Physical Review B **80**, 035310 (2009).

[29] D. Q. Wang, J. C. H. Chen, O. Klochan, K. Das Gupta, D. Reuter, A. D. Wieck, D. A. Ritchie, and A. R. Hamilton, Influence of surface states on quantum and transport lifetimes in high-quality undoped heterostructures, Phys. Rev. B **87**, 195313 (2013).

[30] P. T. Coleridge, R. Stoner, and R. Fletcher, Low-field transport coefficients in GaAs/$Ga_{1-x}Al_xAs$ heterostructures, Physical Review B **39**, 1120 (1989).

[31] In ref. [19] the 3D variant of the Lifshitz-Kosevich formula, valid for 3D bulk materials, has been used to analyse their 2D electron system.

[32] P. T. Coleridge, Small-angle scattering in two-dimensional electron gases, Physical Review B **44**, 3793 (1991).

[33] We leave the explanation of the bad IMEC Dingle plots to future work. They may be related to a sub-optimal Hall bar geometry which distorts equipotential lines at finite B. A possible cause may also be related to the positive background magnetoresistance.

[34] See ref. [32] for discussion of Dingle plots with bad intercepts. In some circumstances, calculating τ_q from such a Dingle plot is still valid.

[35] F. Stern and W. E. Howard, Properties of semiconductor surface inversion layers in the electric quantum limit, Physical Review **163**, 816 (1967).

[36] R. Winkler, S. Papadakis, E. De Poortere, and M. Shayegan, *Spin-orbit coupling in two-dimensional electron and hole systems*, Vol. 41 (Springer, 2003).

[37] The interaction potential in ref. [20] (eq. 13) uses the silicon permittivity κ_{si} rather than the average permittivity $\overline{\kappa}$ [35, 38]. (The usage of $\overline{\kappa}$ correctly accounts for interactions involving image charges in the silicon oxide, as well as charges in the substrate).

[38] T. Ando, Screening effect and quantum transport in a silicon inversion layer in strong magnetic fields, Journal of the Physical Society of Japan **43**, 1616 (1977).